## ORIGINAL ARTICLE

# Cerebral vascular leak in a mouse model of amyloid neuropathology

Eric A Tanifum[1,5], Zbigniew A Starosolski[1,2,5], Stephanie W Fowler[3], Joanna L Jankowsky[3,4] and Ananth V Annapragada[1]

In Alzheimer's disease (AD), there is increasing evidence of blood–brain barrier (BBB) compromise, usually observed as 'microbleeds' correlated with amyloid plaque deposition and apoE-ε4 status, raising the possibility of nanotherapeutic delivery. Molecular probes have been used to study neurovascular leak, but this approach does not adequately estimate vascular permeability of nanoparticles. We therefore characterized cerebrovascular leaks in live APP + transgenic animals using a long circulating ~100 nm nanoparticle computed tomography (CT) contrast agent probe. Active leaks fell into four categories: (1) around the dorsomedial cerebellar artery (DMCA), (2) around other major vessels, (3) nodular leaks in the cerebral cortex, and (4) diffuse leaks. Cortical leaks were uniformly more frequent in the transgenic animals than in age-matched controls. Leaks around vessels other than the DMCA were more frequent in older transgenics compared with younger ones. All other leaks were equally prevalent across genotypes independent of age. Ten days after injection, 4 to 5 µg of the dose was estimated to be present in the brain, roughly a half of which was in locations other than the leaky choroid plexus, and associated with amyloid deposition in older animals. These results suggest that amyloid deposition and age increase delivery of nanoparticle-borne reagents to the brain, in therapeutically relevant amounts.

## INTRODUCTION

Permeability of the blood–brain barrier (BBB) is a key requirement for the transport of exogenous molecular or particulate species between the blood and the brain parenchyma (e.g., therapeutic drugs or imaging agents). In healthy individuals, the BBB is relatively impermeable due to tightly packed endothelial cells that line the brain vasculature. However, the integrity of the BBB can be compromised by neurodegenerative disease and BBB abnormalities have been reported in Alzheimer's disease (AD) dating back to the original studies by Alzheimer.[1] It has been suggested that the neovascularization observed by Alzheimer may have actually resulted from collateralization around cerebral infarcts.[2] The incomplete endothelial layer in newly formed vessels would render these areas susceptible to increased BBB penetration. Recent work has shown BBB dysfunction in both AD and vascular dementia, where microhemmorhage has been detected in 30% of patients with AD and up to 80% of those with cerebral amyloid angiopathy (CAA).[3,4] The presence of leaks in the BBB has obvious implications for the delivery of therapeutic molecules and imaging agents to the brain. In the case of AD, it suggests that enhanced permeability of the BBB may increase the transport efficiency of systemically administered drugs. It is yet unclear whether these leaks are causative of, consequential to, or irrelevant to AD.[5–8] An understanding of the cerebral vascular leak process in AD is therefore of interest.

Blood–brain barrier dysfunction has also been reported in the general aging population. The Rotterdam study[9] found a high prevalence of cerebral microbleeds across the aging population, increasing from 17.8% at age 60 to 69 to 38.3% in those over 80. Microbleed prevalence in patients with symptomatic intracranial hemorrhages ranges from 20% to 70%.[10,11]

Microbleeds have been associated with disruption of the endothelium and vascular basement membrane,[12] and the deposition of prothrombin and hemosiderin in the extravascular space.[13,14] Several causes for AD-associated microbleeds have been proposed. Amyloid deposition may promote apoptosis of vascular endothelial cells through contact with amyloid-β peptide.[15] Local Aβ levels have been correlated with the depletion of smooth muscle cells in large blood vessels and the loss of endothelium in smaller vessels.[2] In mouse models, BBB permeability increases before plaque formation.[16] In the case of CAA, deposition of Aβ plaques in the leptomeningeal arterioles has led to the suggestion that the deposits themselves cause the leak.[17] The apoE-ε4 allele, a significant risk factor for AD, has also been associated with increased vascular leak.[14,18,19] Mechanistically, pericyte deficiency and detachment from the basement membrane have been suggested as triggering events leading to the leak.

Of recent interest, intravenously injected nanoparticle agents have successfully labeled amyloid plaques,[20–23] but their mechanism of transport across the BBB is unclear. Nanoparticle delivery

to the central nervous system occurs without any permeability enhancers or active transport mechanisms, suggesting it may be mediated by passive vascular leak. The majority of past studies of vascular leak have used molecular probes to detect extravasation (e.g., Evans blue, magnetic resonance contrast agents, or a radiotracer),[24,25] the largest molecules investigated have been dextrans, around 100 kD. Such studies are not reflective of nanoparticle delivery for two reasons: (1) nanoparticles are typically much larger with molecular weights in the 100-MD range and (2) both BBB permeation and postextravasation transport are likely to be size dependent. We therefore chose to study the distribution of cerebral vascular leaks *in vivo* using an X-ray opaque liposome that we have used extensively as a blood pool and leakage evaluation agent in previous studies.[26–29]

We used the tet-off APP model of Alzheimer's-like amyloid neuropathology,[30] offering three advantages for the current experiments. First, because it encodes two familial mutations in the APP transgene, it develops aggressive amyloid pathology that becomes severe by the late ages studied here. Second, the mice develop CAA alongside parenchymal amyloid deposits, mimicking the vascular disruption of AD. Finally, transgene expression in this model can be controlled with oral doxycycline, which can be used to avoid side effects of APP overexpression during postnatal brain maturation. We used X-ray computed tomography (CT) to evaluate central nervous system access of peripherally administered nanoparticles with an eye toward the development of both future imaging agents and therapeutic delivery vehicles.

## MATERIALS AND METHODS

### Mice
All animal studies reported in this paper were conducted under study-specific protocols that were approved by the IACUC (Institutional Animal Care and Use Committee) at Baylor College of Medicine and Texas Children's Hospital. The studies reported in this paper are in accordance with the NC3RS ARRIVE guidelines.

The tet-responsive APP transgenic line 102 (tetO-APPswe/ind 102; MMRRC stock # 034845-JAX[30] and the tet-activator line B CaMKIIα-tTA (Jackson Laboratories #3010[31] were independently backcrossed to C57BL/6J for >25 generations before being intercrossed for these studies. The resulting double transgenic male offspring were then mated with wild-type FVB females to produce experimental cohorts on an FVBB6 F1 background. The tet-off amyloid deposition characteristics and quantitative measures of amyloid burden of this mouse line were previously studied.[32] A total of 16 APP+ (6 younger than 10 months, 10 older than 14 months) and 19 APP− (6 younger than 10 months, 13 older than 14 months) animals were imaged. Of these, one of the <10Mo APP+ animals died unexpectedly during the imaging procedure. Another <10Mo APP+ animal was scanned successfully but the images were found to be blurred due to unexpected animal motion during the scan. These two data sets were therefore not used, leaving a total of 14 APP+ and 19 APP− animals whose data were used. Of these, 4 APP+ and 6 APP− animals were under 10 months of age, while the remaining 10 APP+ and 13 APP− animals were older than 14 months.

### Doxycycline Administration
All mice used in this study were raised on doxycycline to suppress transgene expression during postnatal development. All mouse feed was obtained from Purina Mills, St Louis, MO, USA. Offspring were started on dox 1 to 3 days after birth by placing nursing mothers on medicated chow, formulated to 50 mg/kg dox (Purina Mills Test Diet #5APL). At weaning, mice were maintained on dox until 6 weeks of age (Purina Mills Test Diet #5SBA). All mice were returned to regular chow to initiate transgene expression for the remainder of the experiment.

### Image Acquisition
*Computed tomography imaging.* An iodinated liposomal *blood pool contrast agent* (BPCA) was used to evaluate leak and visualize the vasculature. Briefly, the BPCA was prepared by hydration of an ethanolic solution of lipids (Dipalmitoyl Phosphatidyl Choline, Distearoyl phosphatidyl-

ethanolamine-methoxy polyethylene glycol, and cholesterol) in an aqueous solution of iodixanol, followed by high temperature (65°C) extrusion through polycarbonate track-etch membranes to downsize the liposomal particles to the desired 100 to 150 nm size. The unencapsulated iodixanol was then removed by diafiltration, and the residual liposomal suspension diluted or concentrated as necessary to the desired iodine concentration (~110 mg(I)/mL). Full details of the preparation are provided elsewhere.[27] All animals received two doses of contrast agent (Day 1 and Day 10, each dose was 20 mL/kg body weight, delivering 2,200 mgI/kg).

Imaging was performed on a Siemens Inveon CT system (Siemens AG, Erlangen, Germany). Animals were anesthetized (4% isoflurane in oxygen in an induction chamber for 5 to 10 minutes, 1.5% to 2% isoflurane in oxygen during imaging, delivered by face-cone). All images were reconstructed at a 35-$\mu$ isotropic resolution. Precontrast images were acquired (70 keV, 500 $\mu$A, 850 ms, 540 projections, ~20 minutes total scan time, estimated radiation dose 2.5 mGy per projection, total 2.7 Gy) on the designated day 1. They were then injected (20 mL/kg) with the contrast agent and returned to their cages for 10 days. During this period, contrast was expected to leak in the areas of active bleeds. At the same time, contrast remaining in the bloodstream was expected to be eliminated *via* reticulo-endothelial clearance. Preliminary studies showed that the BPCA was detectable above the background for up to 8 days. The mice were therefore imaged on day 11 at high resolution (70 keV, 500 $\mu$A, 850 ms, 1,440 projections, ~56 minutes scan time, estimated radiation dose 8.7 mGy per projection, total 12.57 Gy). They were then reinjected with the BPCA and imaged again at high resolution to record the vasculature. The animals were then killed and their brains excised for histologic evaluation. To verify that the precontrast scan radiation dose did not induce any of the observed leaks, a control group of animals was injected with contrast and returned to their cages without any scanning performed, and imaged 11 days after injection in a manner identical to the experimental animals.

### Image Processing
*Volume registration.* Precontrast images depict the cranium and intracranial radioopaque features such as calcifications, while soft tissue and blood are not well visualized. Acute-phase postcontrast images show blood vessels ranging in diameter from 45 $\mu$m (e.g., the pontine arteries arising from the basilar) to 2 to 3 mm (jugular veins). Delayed-phase postcontrast images show the locations of vascular leak. To facilitate detailed comparisons of these images, we masked high-intensity bone for each scan and used these masks to manually register the volumes with the Slicer3D software (http://www.slicer.org). Since there was no shape change between the three scans of a single animal, affine transformations (rotation and translation) were sufficient to register the images. On the basis of the mask, the skull was then digitally subtracted from each volume.

*Leak classification.* Registered volumes were reviewed by a trained observer. To avoid bias, the reviewer was blinded to the genotype and treatment group for each animal. Leaks were observed in the delayed phase (10-day) images and classified into four categories: (1) Leaks along vessels. These leaks were obviously along a blood vessel in the brain as observed in the CT images. They were not consistently along any particular vessel, but were essentially random. (2) Leaks around the dorsomedial-cerebellar artery (DMCA) within the choroid plexus. These were similar to category 1, but were specifically along the DMCA, and were consistently present along this vessel in all the mice. They were therefore separated as a category. (3) Spherical leaks in cerebral cortex. This area corresponded to a high density of amyloid plaque deposition, and these spherical leaks, with distinct morphology were present there, but had no obvious association with a blood vessel in the CT images. (4) Diffuse leaks not fitting in any of the first three categories. To objectively quantify these visually identified leaks, we created the following procedure. First, subvolumes containing the leaks were marked, and then cropped with a clear margin of surrounding tissue. Representative subvolumes of normal tissue were identified visually, and the background noise in these subvolumes was approximated by a Gaussian distribution.[33,34] The marked subvolumes containing leaks were then thresholded to the noise-mean + 3s.d.. Each voxel with intensity level greater than the threshold was counted as part of the leak, and the threshold-subtracted intensity counted as the leak intensity. Total leak volume was calculated by summing the number of voxels that were within the leak.

*Statistical analysis.* Leaks in the APP+ and APP− mice were compared based on their volume and integrated intensity (Supplementary Figures S1

and S2). Leak volume was measured as the number of voxels registering intensities above the 3s.d. threshold, and scaled to mL units using the 35-$\mu$ voxel edge dimension. Integrated intensity was measured as the sum of intensities (HU) of all voxels in the leak volume. Using the known opacity of iodine ($\sim 46$ HU/mgI/mL), the amount of iodine in each leak was estimated (Figure 2). To evaluate the effect of age, each group (APP+ and APP−) was subdivided by age into <10Mo and >14Mo subgroups and the leak volume and iodine present in each leak were calculated and compared (Supplementary Figures S3 and S4). In all cases, the Kruskal–Wallis test was used to assess differences between groups.

### Histologic Examination

*Tissue preparation and gelatin embedding.* At the conclusion of imaging, animals were overdosed with pentobarbital and transcardially perfused with cold phosphate-buffered saline (PBS) followed by 4% paraformaldehyde. Brain tissue was postfixed by immersion in 4% paraformaldehyde for 48 hours, and cryoprotected in 30% sucrose/PBS at 4°C for >1 week. Tissue was then aligned in the flat skull position and bisected coronally at approximately −4.16 mm from bregma.[35] Tissue was prepared for embedding by incubating for 2 hours at 37°C in 5% gelatin/PBS (Sigma, G2500, Sigma Aldrich, St. Louis, MO, USA), followed by 2 hours at 37°C in 9% gelatin/PBS. Tissue was then placed cut-face down onto a slab of solidified gelatin inside a plastic mold and flooded with 11% gelatin until submerged. After hardening at room temperature, blocks were removed from the mold and refixed overnight in 4% paraformaldehyde and reprotected for 24 hours in 10% sucrose/PBS followed by 3 days in 30% sucrose/PBS, all at 4°C.

*Tissue sectioning.* Tissue blocks were trimmed to remove excess gelatin and marked at one corner for orientation before being submerged in prewarmed 2% gelatin/PBS within a peel-away plastic mold (Polysciences, 18646A-1, Polysciences, Warrington, PA, USA) and frozen by submersion in isopentane chilled to −60°C. Frozen blocks were sectioned at 40 $\mu$m in the coronal plane using a freezing-sliding microtome. Sections were stored in cryoprotectant (0.1 mol/L phosphate buffer pH 7.4, 30% ethylene glycol, 25% glycerol) at −20°C until use.

*Histology.* For all stains, gelatin-embedded sections were washed in Tris-buffered saline before being mounted on Superfrost Plus slides (Fisher Scientific, Waltham, MA, USA) and dried overnight at room temperature. Before staining, sections were rehydrated in running tap water for 20 minutes, dehydrated through alcohols and xylene, and then rehydrated through the same series (except for Thioflavine, which was stained without dehydration). Once staining was complete, sections were dehydrated through alcohols and xylene and coverslipped in Permount (Fisher Scientific).

*Cresyl violet stain.* Sections were stained with 0.1% cresyl violet acetate (Sigma, 860980) for 5 minutes and differentiated in 95% ethanol containing 10% glacial acetic acid.

*Thioflavine-S stain.* Sections were pretreated by incubation in 0.25% KMnO$_4$ (J.T. Baker, 3232-01, Avantor Performance Materials, Phillipsburg, NJ, USA) for 5 minutes, followed by 1% K$_2$S$_2$O$_5$ (Sigma, P2522) containing 1% oxalic acid (J.T. Baker, 0230-01) for 5 minutes, before being stained in 0.02% Thioflavine-S (Sigma, T1892) for 8 minutes. Sections were differentiated in 80% ethanol, followed by slow running tap water.

*Perls Prussian blue.* All glassware used for Perls staining was washed in concentrated nitric acid and rinsed in running distilled water before use. Sections were stained in a freshly prepared mixture of 2% hydrochloric acid and 2% potassium ferrocyanide for 45 minutes at room temperature with gentle agitation, followed by a thorough rinse in several changes of distilled water.

*von Kossa stain.* Tissue was stained using a von Kossa kit according to the manufacturer's instructions (American Mastertech, #KTVKO, American Master Tech, Lodi, CA, USA). Slides were incubated in 5% aqueous silver nitrate solution in full spectrum UV light for 2 hours and rinsed several times in distilled water. The remaining unreacted silver was removed by incubating in 5% thiosulfate for 5 minutes with gentle agitation followed by several rinses in distilled water.

## RESULTS

### The Prevalence of Microbleeds

Figure 1 shows an overview of the CT imaging results in this study. Computed tomography images were collected at three timepoints: precontrast, 10 days after contrast injection ('10-day-post') and immediately after contrast injection, on the same day as the 10-day post ('10-day-acute'). Thus, the prescan images show only endogenous radioopaque structures (Figures 1A, 1D, 1G, and 1J), while the 10-day postinjection images show the sites of vascular leak where contrast accumulates (Figures 1B, 1E, 1H, and 1K). The 10-day-acute images show both vascular structures and leaks (Figures 1C, 1F, 1I, and 1L). Precontrast, the only visible features other than bone are hyperintense spots in the thalamus, ventral to the hippocampus (Figures 1D to 1F). Such structures have been previously attributed to amyloid overproduction.[36] In our study, these structures do not appear to be associated with any active vascular leaks as they do not exhibit emergent signal in the 10-day-post images. However, numerous new intensities appear in the 10-day-post images that can be attributed to fresh vascular leaks. Supplementary Movie M1 shows a volume rendering of all these structures in relation to each other. The observed leaks can be divided into four categories:

- Spherical leaks in the cerebral cortex, not obviously associated with any major vessels in the CT images (Figures 1E and 1F).
- Leaks in the choroid plexus, particularly along the DMCA (Figures 1K and 1L).
- Leaks along other vessels (Figures 1H and 1I).
- Sporadic leaks that do not appear to fit into any of these categories, and with no obvious classification.

Signal enhancement is also observed in several locations close to the surface of the skull, consistent with leaks in pial vessels. Cerebral amyloid angiopathy in pial vessels is observed in this model under histologic examination (e.g., Figures 5F and 5G). However, the proximity to the highly X-ray absorptive skull makes it difficult to unequivocally classify these as leaks. We therefore do not include them in the current analysis. If they are indeed leaks, then it would mean the BBB permeation by the probe particles is even higher than estimated in the current analysis.

A comparison between minimal X-ray dose ('radiation control') and the higher dose associated with repeat scanning showed no consistent relationship between the radiation dose and leak prevalence. Changes observed between these conditions (both increases and decreases) were not significant at the 95% confidence level (Supplementary Figures S1 and S2). Animals that underwent the precontrast scan were therefore pooled with those that did not undergo precontrast scanning to quantify the dependence of leak on genotype.

Leaks were quantified by the leak volume and total payload delivered (Figure 2). (For the purposes of this study, payload was defined as the encapsulated contrast agent: iodixanol.) As noted in Figure 2A, all animals (13/13 APP+ and 17/17 APP−) exhibited vascular leaks. Similarly, 12/13 APP+ and 17/17 APP− animals showed leaks along the DMCA, suggesting that these leaks were independent of genotype. Spherical leaks in the cortex were present in practically all (12/13) APP+ animals, but only in one (1/17) APP− animals. Diffuse or miscellaneous other leaks were a minor contribution to the overall leak, and were sporadically present (5/13 APP+ and 4/17 APP−). The leaks in the DMCA were the largest, followed by those along other vessels, spherical leaks in the cortex and other miscellaneous leaks, in that order.

Comparison of leak volume between the APP+ (amyloid-bearing, $n = 13$) and APP− animals (control, $n = 17$) shows a statistically significant difference between genotypes only for spherical leaks in the cortex ($P < 0.01$). Tissue collected at necropsy was used to confirm the presence of cortical vascular leaks in the
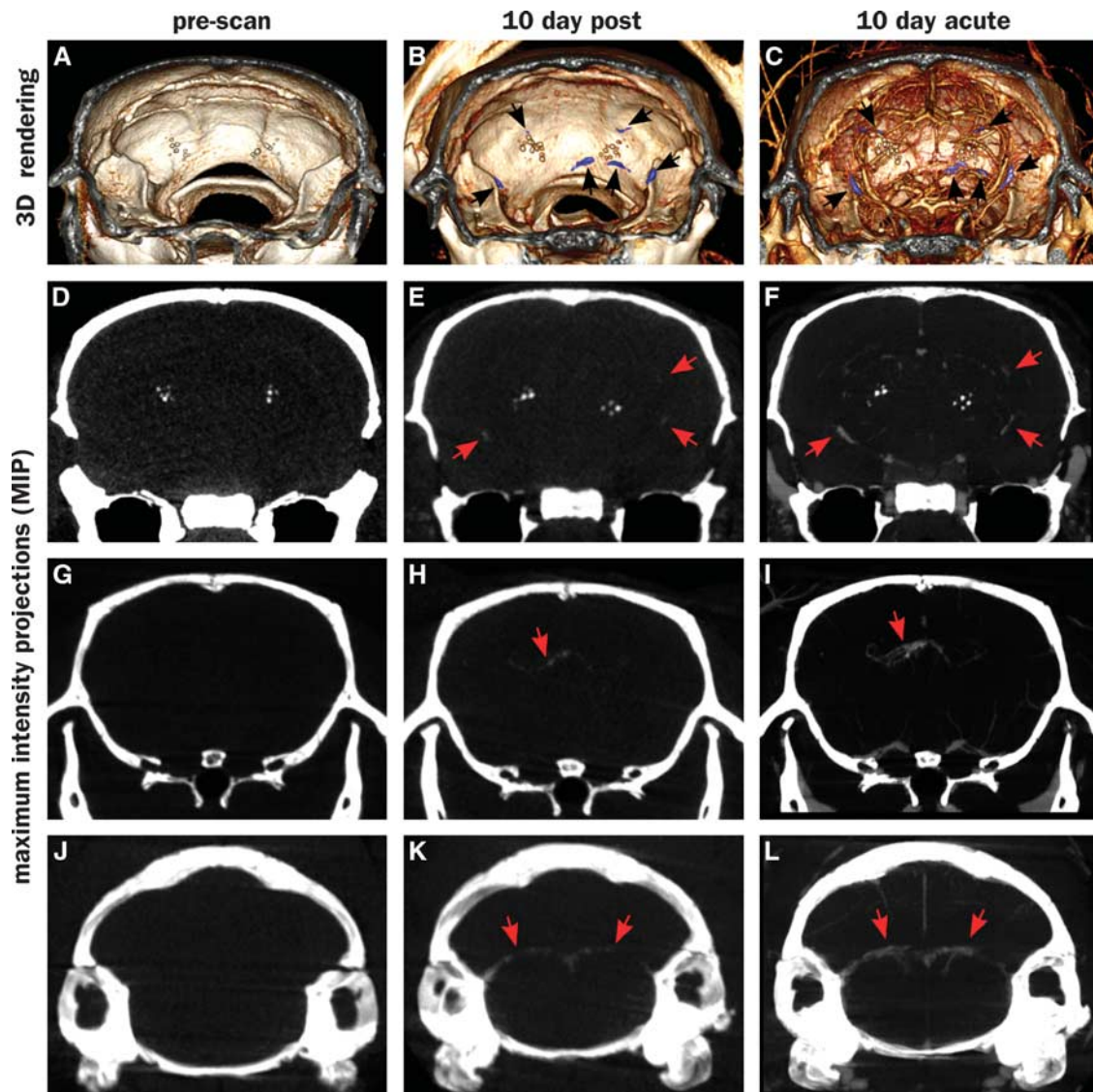
**Figure 1.** Vascular leaks along vessels in computed tomography (CT) scans of an APP+ >14Mo animal. First row (A–C): volume renderings showing an intracranial slab of 8 mm thickness, black arrows point to leaks (colored blue). Rows 2 through 4 (D–L) show maximum intensity projections (MIPs) of a 5-mm slab with the same midpoint. Leaks are not visible in prescans (A, D, G, and J), but are visible in 10 day postinjection scans (B, E, H, and K). Acute scans performed immediately after reinjection of the contrast agent allow localization of the leaks (visualized by nanoparticle injection 10-days prior) to the vasculature (visualized by circulating nanoparticles injected minutes earlier; C, F, I, and L). Bright spherical structures in volume rendering and MIP images are calcospherites described further in Figures 4 and 5. Supplementary Information module M1 is a video showing these leaks in relation to blood vessels.

insular and motor cortex of APP+ mice where leaks were observed. Perls Prussian blue stain revealed hemosiderin deposits throughout the cortex (Figures 3A to 3D). In most of the animals, staining was infrequent, with only 1 to 2 bleeds seen per section, consistent with previous studies of this model.[37] The bleeds were generally small, and limited to the immediate vicinity of small cortical blood vessels. By visual observation, the number of spherical leaks is far smaller than the number of amyloid plaques suggesting that not all plaques cause leaks, but the leaks are probably caused by the plaques or CAA.

Stratification of the mice by age (Supplementary Figure S3) reveals that the leaks along vessels (excluding those along the DMCA) increase significantly with age in the APP+ mice alone. APP+ mice >14 months of age have significantly more leaks than APP+ mice <10 months of age. However, there is no difference between APP+ and APP− mice older than 14 months,

suggesting that the increase in leak may be part of the aging process, and not necessarily related to amyloid deposition.

Identical trends were observed in the amount of iodixanol that was deposited in the tissue (Figure 2B; Supplementary Figure 4). The data suggest that at the time of observation (10 days after injection), a total of 4 to 5 $\mu$g iodixanol was present in the brain. In APP+ animals, about half of this amount was associated with the DMCA and in the choroid plexus. However, the remaining half was associated with vascular leaks in the cerebral cortex and diffuse leaks throughout the brain.

### Persistent Computed Tomography Hyperintensities Are Identified as Calcosphrite Deposits Rather than Amyloid

Thalamic hyperintensities were detected by CT with the following frequencies: 3/4 APP+ <10Mo, 9/9 APP+ >14Mo, 0/6 APP−
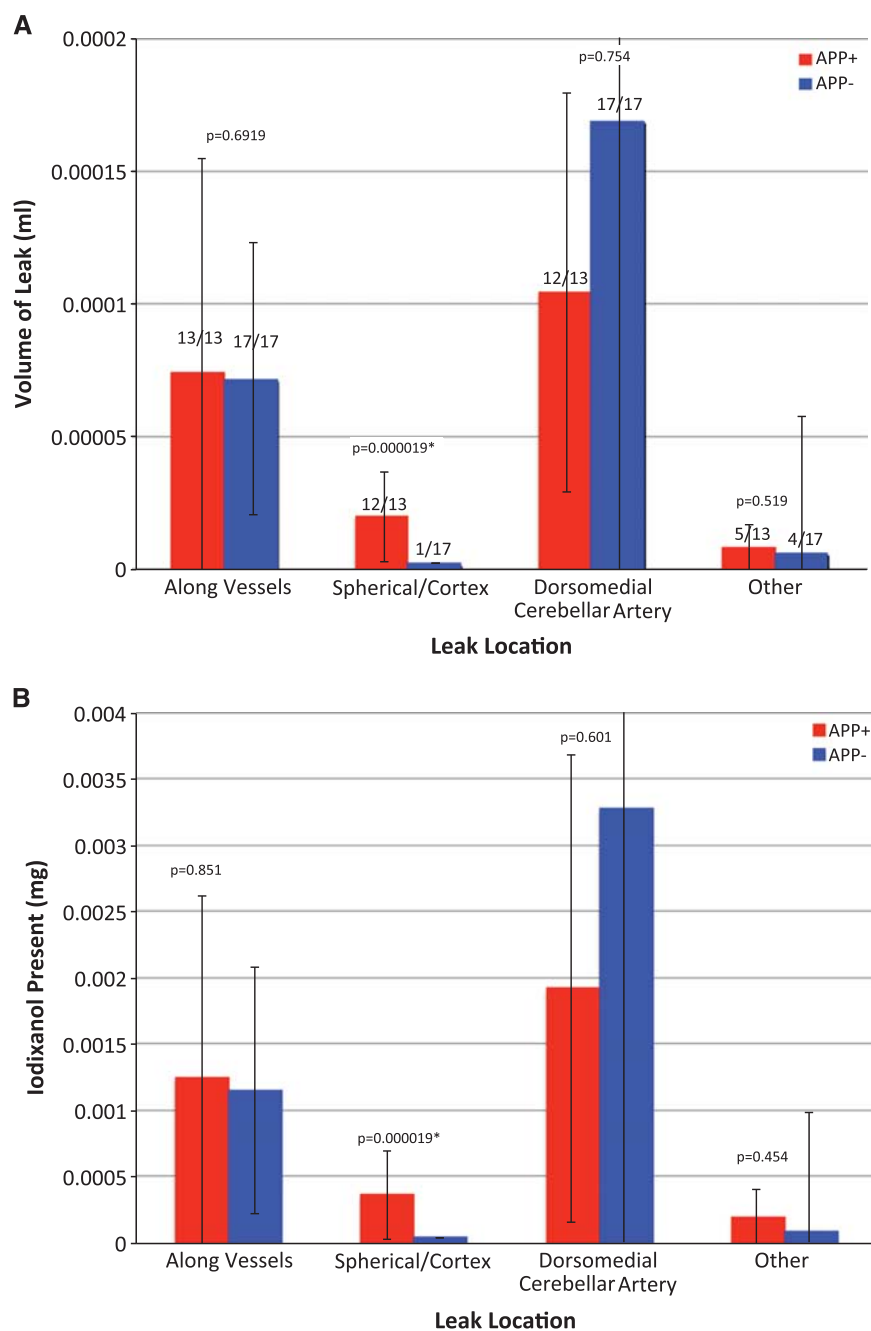
**Figure 2.** (**A**) Mean volume of vascular leaks per mouse as measured by nanoparticle contrast extravasation. All images were reconstructed at 35 $\mu$m voxel resolution. Leaks are defined as the number of voxels with intensity greater than the background mean + 3s.d. and converted to absolute volumes using the 35-$\mu$ voxel size. Typical leaks encompassed thousands of voxels. Note that leaks associated with vessels were present in practically all animals (numbers above bars) while spherical cortical leaks were present in practically all APP + mice but in only 1/17 APP − mice. (**B**) Estimated payload delivery within the leaks. The HU within the voxels of each leak were summed and multiplied by leak volume, and converted to mg Iodixanol/mL using a conversion factor of 22.5 HU/mg/mL of iodixanol. Red bars: APP +, $n = 13$; blue bars: APP −, $n = 17$. Error bars represent the standard deviation of the measurement. The Kruskal–Wallis test was used to determine statistical significance of the differences between APP + and APP − groups. Values of *P* reported on the graphs represent the probability that the two groups are members of identical populations.

<10Mo, 9/11 APP − >14 Mo. Thalamic signal was more intense in older, APP + animals (Figure 4). Although past studies have suggested that this thalamic signal is caused by deposited amyloid, its presence in APP − animals, and indeed, its visibility on CT, indicates the presence of calcium rather than protein. Histologic staining indicated that the deposits are mineral calcospherites rather than peptide fibrils. Unlike amyloid plaques, which become pink when stained with cresyl violet (Figures 5A to 5C), the thalamic deposits appeared darkly stained (Figures 5A, 5B, and 5D). Further, the thalamic deposits were globular in shape, whereas amyloid deposits were distinguished by a characteristic starburst-like appearance. We tested additional sections with von
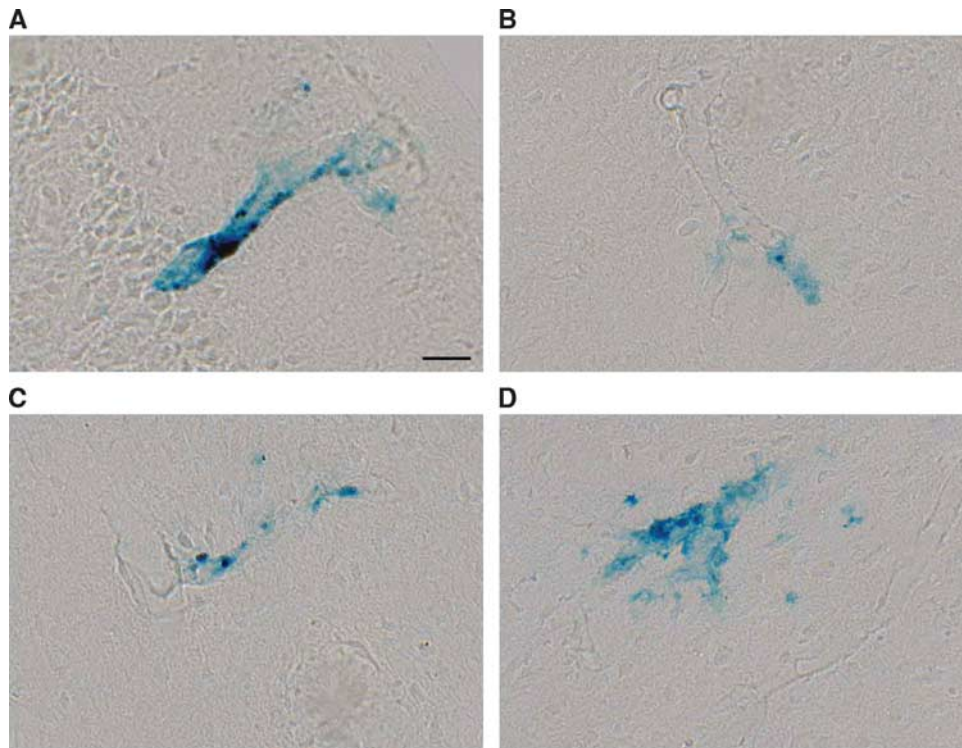
**Figure 3.** Cortical microhemorrhages were detected by Perls Prussian blue staining. Representative vascular leaks identified in insular (**A** and **B**), secondary motor (**C**) and primary motor (**D**) cortices. Scale bar = 25 μm. Examples shown are from an APP+ >14Mo mouse, and representative of observations in APP+ mice in general.
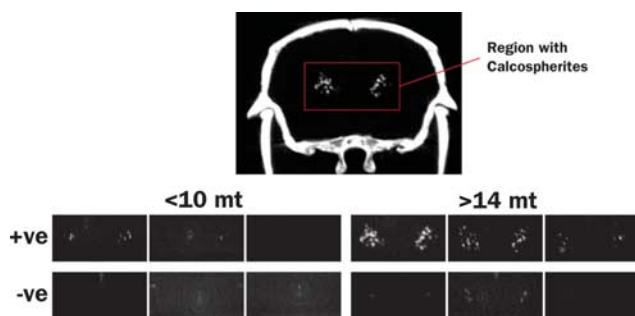


**Figure 4.** Maximum intensity projections of computed tomography (CT) images showing the regions where calcospherites are typically observed. Test animals are grouped as younger (<11 months) and older (>14 months), and by APP transgene status (+ve and −ve). Calcospherites were observed in 3/4 APP+ <11Mo, 9/9 APP+ >14Mo, 0/6 APP− <11Mo, and 9/11 APP− >14 Mo mice, and are obviously more intense in older, APP+ mice.

Kossa stain to confirm mineralization in the thalamus. As predicted, these deposits were stained dark by the von Kossa stain (Figure 5E). Counterstaining of the von Kossa sections with thioflavine-S clearly distinguished amyloid plaques from calcospherites (Figures 5F and 5G). In sum, these findings suggest that mineralized deposits visible by CT are not uncommon in aged animals, but unlike amyloid, are localized primarily to the thalamus and present in both transgenic and control mice. Amyloid deposits are clearly more prevalent than the calcospherites, consistent with our previous observations of amyloid deposition in this mouse line.[32]

## DISCUSSION

The transport of small molecules and nanoparticles from the bloodstream into the brain is of paramount importance for delivery of drugs and diagnostic contrast agents. Past studies in this area have focused primarily on the delivery of chemotherapeutic agents for the treatment of brain cancers, or on small molecule probes for visualization of BBB leak, typically in younger mice. Our own studies of cerebral vasculature using nanoparticle agents, e.g.[38], also studied younger mice. However, with the development of novel therapeutic and diagnostic imaging agents for AD, there is a significant interest in understanding the BBB permeability of nanoparticles, in older animals with amyloid deposition. Here, we have set out to bridge this gap by investigating the BBB penetration of a liposomal nanoparticle probe in a mouse model for AD, at older ages. It is apparent from this study that the BBB is leaky in this model, in four distinct locations: (1) in vessels of the choroid plexus particularly the DMCA, (2) around other vessels throughout the brain, (3) nodular leaks in the cerebral cortex of APP+ animals, and (4) sporadic, diffuse leaks throughout the brain. On the basis of our observations of hemosiderin deposition, and the broadly accepted appearance of 'microbleeds' in human AD patients, we believe that these are physical leaks, where the vascular wall is sufficiently compromised that blood and its constituents can flow through the wall, driven by hydrodynamic forces, without the need for any active transport mechanism.

A striking feature in the brains of these animals is the presence of radioopaque particulate structures in the thalamus, ventral to the hippocampus (Figures 1D to 1F and 2). These structures have been described previously,[36] and were present in mice with mutant APP and PSEN1 genes, but not in mice with mutant PSEN1 alone. They were therefore attributed to APP overexpression, a conclusion that was supported by the identification of Aβ plaques
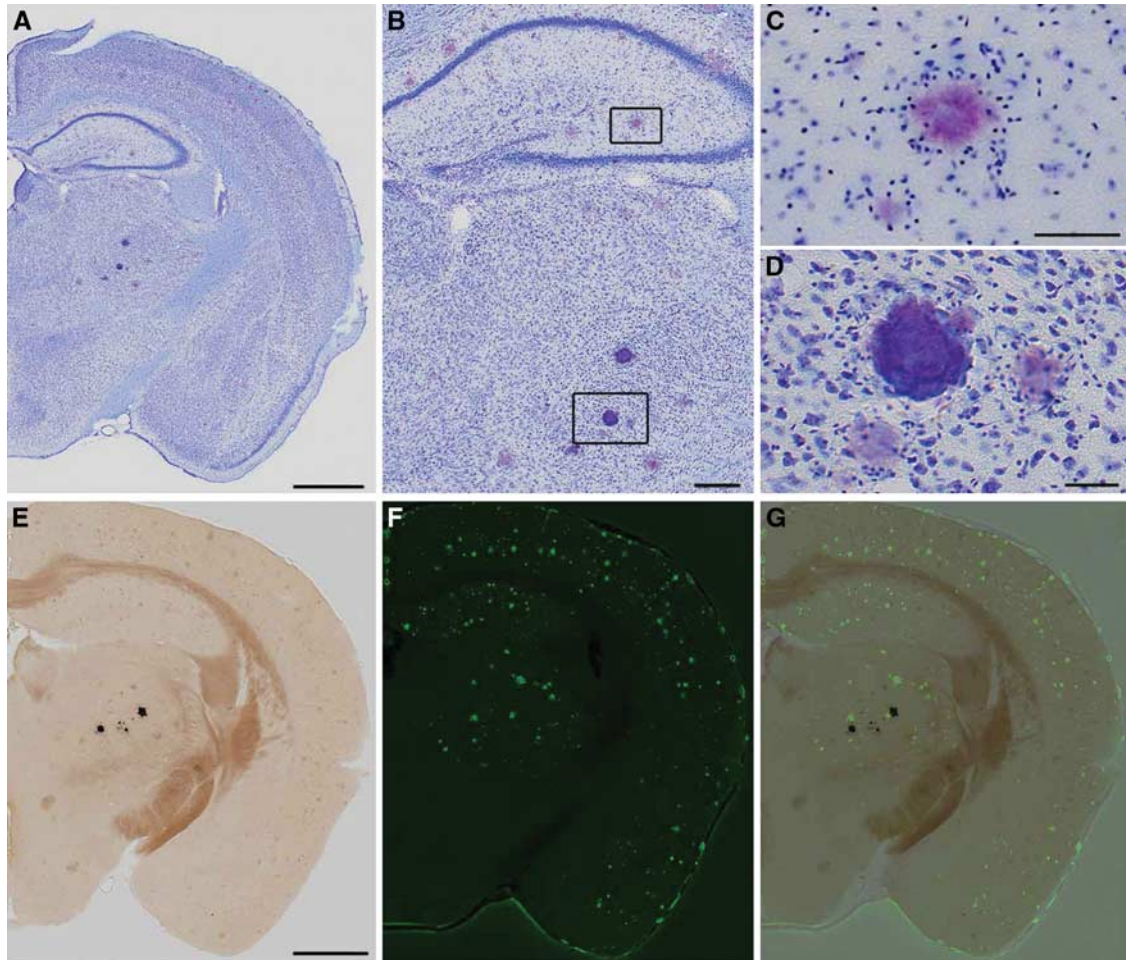
**Figure 5.** (**A**) Coronal sections from APP + mice were stained with cresyl violet to evaluate histopathology areas where thalamic computed tomography (CT) hyperintensities were detected. Thalamic deposits were easily identified by their deep purple color with this stain. (**B–D**) At higher magnification, amyloid plaques display a characteristic starburst shape in Nissl-stained tissue (**C**) while calcospherites are distinguished by their globular morphology (**D**). (**E–G**) Serial tissue sections were stained with von Kossa's method (**E**) and thioflavine-S (**F**) to evaluate coincidence of calcospherites with amyloid. Mineralizations appear black in von Kossa-stained sections and do not overlap with thioflavine-S-stained plaques in green (**G**). Scale bars: (**A** and **E**) 1 mm; (**B**) 500 $\mu$m; (**C** and **D**) 50 $\mu$m. Examples shown are from an APP + >14Mo mouse, and representative of observations in APP + mice in general.

within the structures. Our results show that these structures are present even in the wild-type siblings of the transgenic mutants, and most prevalent in older animals. Most importantly, the structures appear to be highly calcified and while A$\beta$ deposits may be present close by, we see no evidence for A$\beta$ within these structures. Finally, and most relevant to the current study, these structures do not appear to be associated with vascular leakage.

Active vascular leaks were found in multiple other locations, with the most prominent ones appearing in the choroid plexus (12/13 APP + animals and 17/17 APP − animals). Focal leaks within the cerebral cortex (where amyloid plaque burden was substantial) were associated with small blood vessels that were not visible on CT, most likely due to limited spatial and contrast resolution. They occurred in 12/13 APP + animals, and only 1/17 of the APP − . Further, the APP + animals exhibit significantly larger leak volumes and payload transport in the cerebral cortex than the control animals, suggesting that spherical cortical leaks are a consequence of amyloid deposition. Other vascular leaks comprised the group with the second largest leak volume and payload delivery. They appeared to be equally prevalent in all mice regardless of genotype (13/13 APP + and 17/17 APP − ),

although when stratified by animal age, these vascular leaks appeared to be significantly more prevalent in older APP + mice than in younger ones.

Because our measurements of leak volume and iodixanol localization were based on a single time point 10 days after injection, it is not possible to accurately estimate the actual delivery of iodixanol to the brain. The residual amount remaining at 10 days after injection result from a balance between the passive leak into and active clearance away from the brain over this time period. However, assuming a positive clearance rate away from the brain, the total amount of iodixanol delivered must exceed the amount present at the 10-day point. The measured amounts are in the order of 4 to 5 $\mu$g, of which about half is attributed to the DMCA in the choroid plexus, and is independent of APP deposition. The remaining half is predominantly associated with other large vessels in the brain, both arteries and veins, and also appears to be independent of APP status with one exception: among APP + mice, the older age group (>14Mo) has significantly more leak than the younger (<10Mo group). However, leak in the older age group is equal to that found in older APP − mice, suggesting that it is a function of

aging. Focal cortical leaks are the one group that appear to be uniquely dependent on APP status, and constitute a small fraction (~10%) of total leak.

Our findings are consistent with past work suggesting that the mouse BBB becomes permeable to peripherally delivered nanoparticles at ages above ~11 months. In earlier studies using an APP/PS1 model of AD, we showed that amyloid-targeted nanoparticles penetrated the BBB and localized to plaques after intravenous injection[20] Interestingly, the nanoparticles did not preferentially target plaques in any particular location in the brain; plaques throughout the hippocampus and cerebral cortex were uniformly labeled. In the present work, we have shown in an independent model of AD that (1) nanoparticles injected intravenously penetrate the BBB and (2) the majority of leak takes place from major blood vessels, particularly in the choroid plexus. This raises the question of how such particles in our earlier study could have transported throughout the brain to uniformly label amyloid plaques in locations far removed from the leak. The diffusion of nanoparticles in the brain parenchyma is not expected to result in more than about 10 to 50 μm of travel before the concentration gradient is equalized. Two possible explanations may exist: (1) Even though the present work only shows major leaks in the choroid plexus and along large diameter vessels, minor leaks from microvessels may exist throughout the cerebral cortex, but not be visible in the current CT scans due to the limited spatial resolution (35 μm isotropic). However, the absence of obvious background signal casts some doubt on this possibility. (2) The dominant leaks are indeed in the choroid plexus and major vessels, from where particles are transported throughout the brain by convective flow of the cerebrospinal fluid. The weakness of this argument is that transport is restricted to the paths of cerebrospinal fluid flow, and no mechanism for transport away from cerebrospinal fluid flow tracts is provided. While the present study confirms the existence of neurovascular leaks sufficient to extravasate detectable levels of nanoparticles, further studies are needed to properly identify and characterize the mechanism of extravasated nanoparticle transport within the brain.

As in the aged human brain, aged mice also show a significant cerebral vascular leak, but only a fraction of the overall leaks appear to be dependent on the presence of amyloid pathology. This suggests that agents injected into the systemic circulation should have ready access to the brain, contrary to the general assumption of an impenetrable BBB. Isolated spherical leaks in the cerebral cortex of APP+ animals were associated with small blood vessels, while leaks found along major vessels in the brain, particularly in the choroid plexus, were not clearly associated with amyloid deposition. A number of calcified, radioopaque deposits in the thalamus appear to have no hemosiderin content, suggesting that they do not contribute to nanoparticle distribution. Our findings have important implications for drug delivery to the brain of aged animals, especially those with amyloid neuropathology: liposomal nanoparticles of the type tested here, i.e., pegylated liposomes, should have ready access to the brain via vascular leak in the choroid plexus, other vascular leaks, in the cerebral cortex and elsewhere. Following such leak, particles will presumably be transported by the glymphatic pathway.[39–41] It is unclear how efficient such transport is, but constitutes one possible mechanism for particle transport to far corners of the brain. Extrapolating our results to the human condition would suggest that older patients with greater amyloid burden could be expected to allow larger amounts of nanoparticles to enter the brain from the vasculature. However, if the quantitative trends were to be applicable in humans, then they would suggest that the increase would only be in the order of about 10%, and that younger patients in earlier stages of the disease would admit almost 90% of the total nanoparticle traffic into the brain, boding well for diagnostic and therapeutic agents even in early stages of the disease.

## DISCLOSURE/CONFLICT OF INTEREST

## REFERENCES

1 Alzheimer A. Uber eine eigenartige Erkrankung der Hirnrinde. *Allgemeine Zeitschrife Psychiatrie* 1907; **64**: 146–148.

2 Kalaria RN. Cerebrovascular degeneration is related to amyloid-β protein deposition in Alzheimer's disease. *Ann NY Acad Sci* 1997; **826**(1 Cerebrovascul): 263–271.

3 Pettersen JA, Sathiyamoorthy G, Gao F-Q, Szilagyi G, Nadkarni St NK, George-Hyslop P et al. Microbleed topography, leukoaraiosis, and cognition in probable Alzheimer disease from the Sunnybrook dementia study. *Arch Neurol* 2008; **65**: 790–795.

4 Skoog I, Wallin A, Fredman P, Hesse C, Aevarsson O, Karlsson I et al. A population study on blood-brain barrier function in 85-year-olds: relation to Alzheimer's disease and vascular dementia. *Neurology* 1998; **50**: 966–971.

5 Cordonnier C, van der Flier WM. Brain microbleeds and Alzheimer's disease: innocent observation or key player? *Brain* 2011; **134**: 335–344.

6 Thijs V. Cerebral microbleeds: important or not important? *Swiss Arch Neurol Psychiatry* 2011; **162**: 290–292.

7 van der Vlies AE, Goos JDC, Barkhof F, Scheltens P, van der Flier WM. Microbleeds do not affect rate of cognitive decline in Alzheimer disease. *Neurology* 2012; **79**: 763–769.

8 Thakker DR, Weatherspoon MR, Harrison J, Keene TE, Lane DS, Kaemmerer WF et al. Intracerebroventricular amyloid- antibodies reduce cerebral amyloid angiopathy and associated micro-hemorrhages in aged Tg2576 mice. *Proc Natl Acad Sci USA* 2009; **106**: 4501–4506.

9 Vernooij MW, van der Lugt A, Ikram MA, Wielopolski PA, Niessen WJ, Hofman A et al. Prevalence and risk factors of cerebral microbleeds: the Rotterdam Scan Study. *Neurology* 2008; **70**: 1208–1214.

10 Koennecke H-C. Cerebral microbleeds on MRI: prevalence, associations, and potential clinical implications. *Neurology* 2006; **66**: 165–171.

11 Viswanathan A, Chabriat H. Cerebral microhemorrhage. *Stroke* 2006; **37**: 550–555.

12 Perlmutter LS, Chui HC. Microangiopathy, the vascular basement membrane and Alzheimer's disease: a review. *Brain Res Bull* 1990; **24**: 677–686.

13 Cullen KM, Kócsi Z, Stone J. Microvascular pathology in the aging human brain: evidence that senile plaques are sites of microhaemorrhages. *Neurobiol Aging* 2006; **27**: 1786–1796.

14 Zipser BD, Johanson CE, Gonzalez L, Berzin TM, Tavares R, Hulette CM et al. Microvascular injury and blood–brain barrier leakage in Alzheimer's disease. *Neurobiol Aging* 2007; **28**: 977–986.

15 Blanc EM, Toborek M, Mark RJ, Hennig B, Mattson MP. Amyloid β-peptide induces cell monolayer albumin permeability, impairs glucose transport, and induces apoptosis in vascular endothelial cells. *J Neurochem* 1997; **68**: 1870–1881.

16 Ujiie M, Dickstein DL, Carlow DA, Jefferies WA. Blood-brain barrier permeability precedes senile plaque formation in an Alzheimer disease model. *Microcirculation* 2003; **10**: 463–470.

17 Dickstein DL, Walsh J, Brautigam H, Stockton Jr SD, Gandy S, Hof PR. Role of vascular risk factors and vascular dysfunction in Alzheimer's disease. *Mt Sinai J Med* 2010; **77**: 82–102.

18 Zlokovic BV. Neurovascular pathways to neurodegeneration in Alzheimer's disease and other disorders. *Nat Rev Neurosci* 2011; **12**: 723–738.

19 Zlokovic BV. Cerebrovascular effects of apolipoprotein E: implications for Alzheimer disease. *JAMA Neurol* 2013; **70**: 440–444.

20 Tanifum EA, Dasgupta I, Srivastava M, Bhavane RC, Sun L, Berridge J et al. Intravenous delivery of targeted liposomes to amyloid-β pathology in APP/PSEN1 transgenic mice. *PLoS ONE* 2012; **7**: e48515.

21 Wadghiri YZ, Li J, Wang J, Hoang DM, Sun Y, Xu H et al. Detection of amyloid plaques targeted by bifunctional USPIO in Alzheimer's disease transgenic mice using magnetic resonance microimaging. *PLoS ONE* 2013; **8**: e57097.

22 Yang J, Wadghiri YZ, Hoang DM, Tsui W, Sun Y, Chung E et al. Detection of amyloid plaques targeted by USPIO-Aβ1-42 in Alzheimer's disease transgenic mice using magnetic resonance microimaging. *Neuroimage* 2011; **55**: 1600–1609.

23 Andrieux K, Couvreur P. Nanomedicine as a promising approach for the treatment and diagnosis of brain diseases: the example of Alzheimer's disease. *Ann Pharm Fr* 2013; **71**: 225–233.

24 LaRue B, Hogg E, Sagare A, Jovanovic S, Maness L, Maurer C et al. Method for measurement of the blood-brain barrier permeability in the perfused mouse brain: application to amyloid-beta peptide in wild type and Alzheimer's Tg2576 mice. *J Neurosci Methods* 2004; **138**: 233–242.

25 Starr JM, Farrall AJ, Armitage P, McGurn B, Wardlaw J. Blood–brain barrier permeability in Alzheimer's disease: a case–control MRI study. *Psychiatry Res* 2009; **171**: 232–241.

26 Kao C-Y, Hoffman EA, Beck KC, Bellamkonda RV, Annapragada AV. Long-residence-time nano-scale liposomal iohexol for X-ray-based blood pool imaging. *Acad Radiol* 2003; **10**: 475–483.

27 Mukundan S, Ghaghada KB, Badea CT, Kao C-Y, Hedlund LW, Provenzale JM *et al.* A liposomal nanoscale contrast agent for preclinical CT in mice. *AJR Am J Roentgenol* 2006; **186**: 300–307.

28 Karathanasis E, Suryanarayanan S, Balusu SR, McNeeley K, Sechopoulos I, Karellas A *et al.* Imaging nanoprobe for prediction of outcome of nanoparticle chemotherapy by using mammography. *Radiology* 2009; **250**: 398–406.

29 Annapragada AV, Hoffman E, Divekar A, Karathanasis E, Ghaghada KB. High-resolution CT vascular imaging using blood pool contrast agents. *Methodist Debakey Cardiovasc J* 2012; **8**: 18–22.

30 Jankowsky JL, Slunt HH, Gonzales V, Savonenko AV, Wen JC, Jenkins NA *et al.* Persistent amyloidosis following suppression of Aβ production in a transgenic model of Alzheimer disease. *PLoS Med* 2005; **2**: e355.

31 Rotenberg A, Mayford M, Hawkins RD, Kandel ER, Muller RU. Mice expressing activated CaMKII lack low frequency LTP and do not form stable place cells in the CA1 region of the hippocampus. *Cell* 1996; **87**: 1351–1361.

32 Rodgers SP, Born HA, Das P, Jankowsky JL. Transgenic APP expression during postnatal development causes persistent locomotor hyperactivity in the adult. *Mol Neurodegener* 2012; **7**: 28.

33 Lu H, Hsiao T, Li X, Liang Z. Noise properties of low-dose CT projections and noise treatment by scale transformations. *IEEE Nuclear Sci Symp Conf* 2001; **3**: 1662–1666.

34 Kittler J, Illingworth J. Minimum error thresholding. *Pattern Recogn* 1986; **19**: 41–47.

35 Franklin K, Paxinos G. The mouse brain in stereotaxic coordinates (3rd ed) with CD-ROM. Librairie Lavoisier: Cachan, France, 2007.

36 Dhenain M, Tannir El Tayara El N, Wu T-D, Guégan M, Volk A, Quintana C *et al.* Characterization of in vivo MRI detectable thalamic amyloid plaques from APP/PS1 mice. *Neurobiol Aging* 2009; **30**: 41–53.

37 Wang A, Das P, Switzer RC, Golde TE, Jankowsky JL. Robust amyloid clearance in a mouse model of Alzheimer's disease provides novel insights into the mechanism of amyloid- immunotherapy. *J Neurosci* 2011; **31**: 4124–4136.

38 Ayyagari AL, Zhang X, Ghaghada KB, Annapragada A, Hu X, Bellamkonda RV. Long-circulating liposomal contrast agents for magnetic resonance imaging. *Magn Reson Med* 2006; **55**: 1023–1029.

39 Xie L, Kang H, Xu Q, Chen MJ, Liao Y, Thiyagarajan M *et al.* Sleep drives metabolite clearance from the adult brain. *Science* 2013; **342**: 373–377.

40 Iliff JJ, Wang M, Liao Y, Plogg BA, Peng W, Gundersen GA *et al.* A paravascular pathway facilitates CSF flow through the brain parenchyma and the clearance of interstitial solutes, including amyloid β. *Sci Transl Med [Internet]* 2012; **4**: 147ra111–1. Available from http://eutils.ncbi.nlm.nih.gov/entrez/eutils/elink.fcgi?dbfrom=pubmed&id=22896675&retmode=ref&cmd=prlinks.

41 Iliff JJ, Lee H, Yu M, Feng T, Logan J, Nedergaard M *et al.* Brain-wide pathway for waste clearance captured by contrast-enhanced MRI. *J Clin Invest* 2013; **123**: 1299–1309.